Role of Electron-Phonon Coupling in the Thermal Evolution of Bulk Rashba-Like Spin-Split Lead Halide Perovskites Exhibiting Dual-Band Photoluminescence

Julian A. Steele*,[1] Pascal Puech,[2] Bartomeu Monserrat,[3] Bo Wu,[4] Ruo Xi Yang,[5] Thomas Kirchartz,[6,7] Haifeng Yuan,[8] Guillaume Fleury,[1] Eduard Fron,[8] Masoumeh Keshavarz,[8] Elke Debroye,[8] Guofu Zhou,[4] Tze Chien Sum,[9] Aron Walsh,[10,11] Johan Hofkens,[8] and Maarten B. J. Roeffaers*[1]

Supporting Information
The Supporting Information is available free of charge on the ACS Publications website at DOI: XXXX
Experimental methods and additional figures and tables.

1) cMACS, Department of Microbial and Molecular Systems, KU Leuven, Celestijnenlaan 200F, 3001 Leuven, Belgium

2) CEMES/CNRS, Université de Toulouse, 29, rue Jeanne Marvig, 31055 Toulouse, France

3) TCM Group, Cavendish Laboratory, University of Cambridge, J. J. Thomson Avenue, Cambridge CB3 0HE, United Kingdom

4) Guangdong Provincial Key Laboratory of Optical Information Materials and Technology & Institute of Electronic Paper Displays, South China Academy of Advanced Optoelectronics, South China Normal University, Guangzhou 510006, P. R. China

5) Molecular Foundry, Lawrence Berkeley National Laboratory, 1 Cyclotron Road, Berkeley, CA, USA

6) IEK5-Photovoltaics, Forschungszentrum Jülich, 52425 Jülich, Germany

7) Faculty of Engineering and CENIDE, University of Duisburg-Essen, Carl-Benz-Straße 199, 47057 Duisburg, Germany

8) Department of Chemistry, KU Leuven, Celestijnenlaan 200F, Leuven, 3001, Belgium

9) Division of Physics and Applied Physics, School of Physical and Mathematical Sciences, Nanyang Technological University, 21 Nanyang Link, Singapore, 637371, Singapore

10) Department of Materials, Imperial College London, Exhibition Road, London SW7 2AZ, United Kingdom

11) Global E3 Institute and Department of Materials Science and Engineering, Yonsei University, Seoul 120-749, Korea

Email: julian.steele@kuleuven.be / maarten.roeffaers@kuleuven.be

ABSTRACT: The optoelectronic properties of lead halide perovskites strongly depend on their underlying crystal symmetries and dynamics, sometimes exhibiting a dual photoluminescence (PL) emission via Rashba-like effects. Here we exploit spin- and temperature-dependent PL to study single crystal $APbBr_3$ (A= Cs and methylammonium; CH_3NH_3) to evaluate peak energy, intensity and linewidth evolutions of the dual emissions. Both materials are identified to have two temperature regimes – above and below approximately 100 K – being governed by different carrier scattering and radiative recombination dynamics. With increasing temperature, high-energy optical phonons (>11 meV) are found to drive energy splitting of the dual bands and electron-longitudinal-optical-phonon coupling dominates the linewidth broadening, with a stronger coupling constant inferred in $CsPbBr_3$ for the spin-split indirect bands (78 meV) compared to the direct one (54 meV). We find the unusual thermal evolution of all-inorganic $CsPbBr_3$ and hybrid $MAPbBr_3$ perovskites are comparable – suggesting A-site independence and dominance of dynamic spin-splitting effects – and are best understood within a framework which accounts for bulk Rashba-like effects.

The interest for solution-processable lead halide perovskites within efficient solar cells[1,2] stems from their promising optoelectronic response to the solar photons and high tolerance to defects[3,4]. This family of semiconductors are increasingly being considered as “soft” solid-state materials[5–7], whereby the fate of photo-generated charges primarily rely on the fundamental carrier-lattice interaction dynamics. For instance, polaron formation – via carrier-longitudinal-optical-phonon (Fröhlich) interactions – within the lattice has been linked to several favourable qualities, like long carrier lifetimes and diffusion lengths[8–10]. Recent indications of spin splitting and indirect tail state formation in lead halide perovskites[11–16] due to Rashba-like effects[17] motivate a reconsideration of how electron-phonon coupling can exist within its perturbed electronic band structure. Universally, for the application of any polar metal halide perovskite, the properties of the free charge carriers and phonon scattering mechanisms are central to its optoelectronic performance at room temperature (RT).

Bulk Rashba-like effects occur in metal halide perovskites via two key ingredients. First, heavy elements, like Pb, introduce strong spin–orbit coupling (SOC) into the electronic structure. Second, the crystal must lack inversion symmetry, so that an effective magnetic field is imposed on electrons by SOC, lifting spin degeneracy and splitting the band electronic structure, as represented in Figure 1. To lose inversion symmetry, both static[18] (i.e. intrinsically non-centrosymmetric) and dynamic[12,13,19] (i.e. fluctuating breaks in symmetry) mechanisms have been proposed, though the full picture is still heavily debated[20]. Consequently, the valence band maxima[21] (VBM) and conduction band minima (CBM) shift away from the high-symmetry points in the Brillouin zone, giving rise to low-energy indirect tail states[11,15] (Figure 1). The shift for Pb-based perovskites in reciprocal space is expected to be larger for the CBM compared to the VBM due to the relative orbital contributions to the band structure[22], producing a low energy (LE) indirect transition alongside a high energy (HE) direct one. Notably, these phenomena constitute a general result within both all-inorganic and hybrid lead halide perovskites, leading to a characteristic dual photoluminescence (PL) emission[11,15] which is better seen at low temperatures[23].

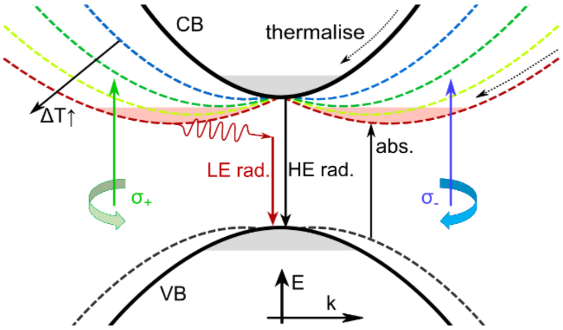

Figure 1: Schematic of energy band structure experiencing thermally-driven Rashba-like spin splitting, with selective excitation provided using left (σ_+) and right (σ_-) circularly polarised light. Photo-generated carriers recombine by two main radiative (rad.) pathways; a high-energy (HE) unperturbed direct bandgap transition, and a phonon-mediated low-energy (LE) indirect bandgap. For simplicity, only the CB splitting shows a thermal dependence.

The origin of the spin splitting in bulk hybrid lead halide perovskites like $MAPbBr_3$ (where MA is methylammonium; CH_3NH_3) is unclear, and is especially puzzling for all-inorganic $CsPbBr_3$, which adopts a centrosymmetric orthorhombic (*Pnma*) crystal structure[24] at RT. However, it is expected that the thermal motion of the Cs^+ atoms (as well as MA molecules) at the cation A-sites couple to lattice vibrations to promote local polar fluctuations[25] (Figure 2a inset) and dynamically break local centrosymmetry[13,16]. It is not known if $CsPbBr_3$ or $MAPbBr_3$ adopt a "static" centrosymmetric structure near 0 K[11]. The intensity of the Rashba-induced LE peak is sensitive to sample preparation[11], being best resolved in large single crystals (SCs)[26]. As such, PL-based studies[27,28] become ambiguous when comparing across different physical microstructures, i.e. nanocrystals or polycrystalline networks. Nevertheless, accounting for Rashba-like effects that underpin the low-temperature dual PL emission in $CsPbBr_3$ and $MAPbBr_3$ will yield a more accurate description of the photophysics involved[29,30].

In this Letter, we report a spin- and temperature-dependent PL analysis of the emission positions, linewidths and intensities arising in SC all-inorganic $CsPbBr_3$ and hybrid $MAPbBr_3$ perovskites possessing dual bands at RT. The two systems exhibit qualitatively similar dependence on temperature, inferring that the underlying models employed are cation-independent. The LE and HE peak positions undergo different evolutions in the lead bromide perovskites, whereby both peaks blueshift when warming above 0 K, with LE undertaking an additional strong redshift above 100 K, assisted by high-energy optical phonons. While high-temperature quenching of the LE emission intensity is in-line with nominal semiconducting behaviour, we assign thermal-driven intersystem crossing to account for a HE intensity which peaks near 100 K and quenches approaching 0 K. The Fröhlich coupling strength of carriers residing in the spin-split bands is found to be much higher than in the direct bands in $CsPbBr_3$, inferred from the temperature-dependent linewidth broadening. We demonstrate that several anomalous features in the low-temperature dual PL emission evolution found in SC $CsPbBr_3$ and $MAPbBr_3$ are best understood when Rashba-like effects are considered.

$APbBr_3$ (A = Cs and MA) SCs were prepared with a modified methods from literature[31], resulting in 1-3 mm-sized perovskite single crystals (Methods and Figure S1 of Supporting Information). Figure 2(a) provides the RT PL spectrum of $CsPbBr_3$, displaying a clear dual emission.[11] At RT, the emission linewidth will be dominated[32] by the Fröhlich interaction strength, represented by dimensionless constant α, which scales with the carrier effective mass (m^*) within the Feynman polaron model[33]:

$$\alpha = \frac{e^2}{\hbar c}\sqrt{\frac{m^* c}{2\hbar\omega_{LO}}}\left(\frac{1}{\varepsilon_\infty} - \frac{1}{\varepsilon_0}\right). \tag{1}$$

Parameters ε_∞ and ε_0 respectively indicate the high-frequency and static dielectric constants, c the speed of light, ħ the reduced Planck constant, e the fundamental charge, and ω_{LO} is the frequency of the coupling optical phonon mode(s) involved. The decisive factor for m^* is the E-k dispersion curvature at the CB and VB extrema (assuming near-parabolic character), whereby: $m^*(k) \propto (\partial^2 E/\partial k^2)^{-1}$.

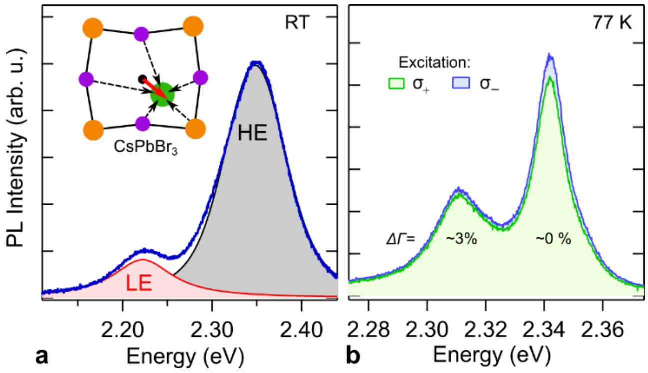

Figure 2: (a) Room-temperature PL spectrum of SC CsPbBr$_3$ ($\lambda_{exc.}$= 400 nm) with dual high- (HE) and low-energy (LE) emissions. The inset illustrates how the perovskite "cage" (Pb-Br framework) and dynamic symmetry breaking[13] of an off-centre Cs cation (green) creates an effective electric dipole moment (solid red arrow), through the summation of local dipoles (dashed arrows). (b) Right circularly polarised PL spectra (77 K) of CsPbBr$_3$ upon exciting (473 nm) with left (σ+) and right (σ-) circularly polarised light. The $\Delta\Gamma$ values depict the difference in the linewidth derived from their fitting: $\Delta\Gamma = 2[\Gamma(\sigma-) - \Gamma(\sigma+)]/[\Gamma(\sigma-) + \Gamma(\sigma+)]$.

Within the spin-split system depicted in Figure 1, a one-band effective mass approximation no longer holds[34] for Equation 1, given two shallow side valleys are formed. For example, carriers thermalizing into each Rashba-induced valley will have nontrivial spin texture, with intervalley scattering mediated via phonons. Importantly, for the spin-split bands, their curvature is expected to be small compared to the direct transition[19,35], indicating an enhancement in the effective mass and a relative increase of the Fröhlich interaction.

The effective mass of charges in the two spin-split indirect bands will evolve as a function of the SOC, described by the Rashba Hamiltonian[34]. Both the electron-phonon coupling[36,37] and the (large) polaronic effective mass[38] correction are enhanced by Rashba-like effects. In this case, the relative electron-phonon coupling strength for carrier in the lower (-) Rashba band are expected to be larger than those in the upper (+) one[38]. As a results, carriers recombining at the two spin-split band edges will encounter different polaron effects, leading to a relatively broader PL emission arising from recombination via the lower branch. We experimentally assess this via a comparison of the LE emission full-width at half maximum (FWHM; Γ) when the recombination has different spin populations, down at cryogenic temperatures (T = 77 K) where the LE band is more pronounced. To exclude instrumental response to light helicity, we fixed the detection optics and only vary the incident polarisation. Figure 2(b) displays right circularly polarised PL spectra recorded from $CsPbBr_3$ using left (σ_+) and right (σ_-) circularly-polarised excitation. Beyond the polarisation-dependence of the emission intensities[11], fitting these data (dual Voigt functions) reveals an approximately 3 % broader LE peak using σ_- excitation compared to σ_+, with no detectable change in the HE linewidth. While this difference is relatively small (the indirect recombination rate will occur relatively slowly compared to the rate of spin-flipping), it is consistent with a relative disparity in the electron-phonon coupling arising from the two spin valleys, and should be enhanced exciting closer to the split band edges[11].

Smearing the spin information, Figure 3(a) overviews the unpolarised temperature-dependence of the normalised PL lineshape in SC $CsPbBr_3$ and $MAPbBr_3$ (raw spectra shown in Figure S2). Besides the asymmetry in the $MAPbBr_3$ HE peak at lower temperatures, the temperature dependence of the two perovskites are comparable, and are evaluated together. Note that fitting the HE band of $MAPbBr_3$ with a second peak to account for the asymmetry yields a comparable thermally-driven trend in the peak position (open circle in Figure 3(b)), suggesting it is related to the direct transition.

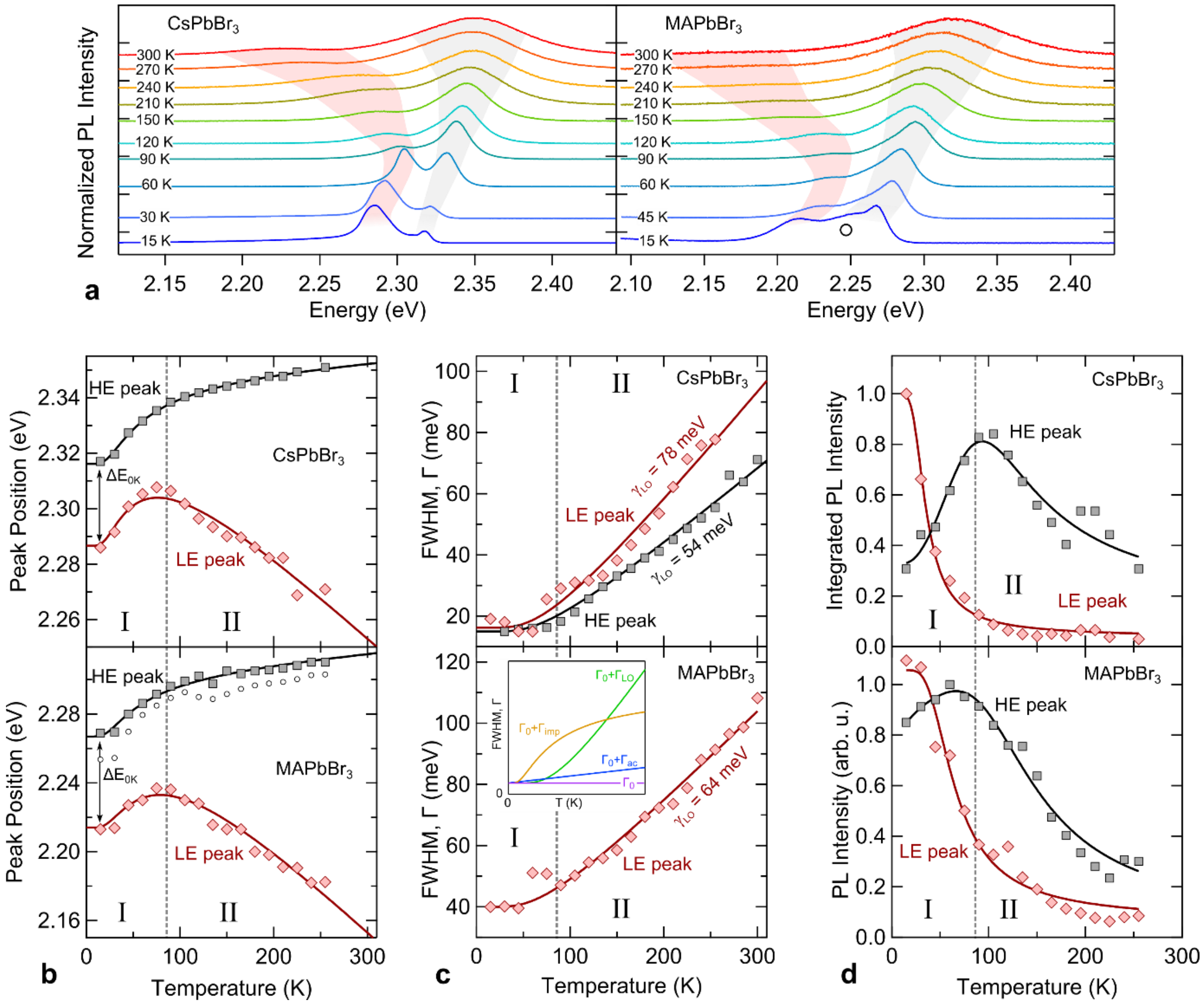

Figure 3: (a) Normalised low-temperature PL spectra of single crystal CsPbBr$_3$ and MAPbBr$_3$ ($\lambda_{exc.}$= 400 nm), with the open circle in the MAPbBr$_3$ data set highlighting the asymmetry seen in the HE peak. Analysis of the temperature evolution for both material systems; (b) Emission peak energies of the peaks, including the third peak identified in (a) by the open circle, modelled using Equation 3; (c) FWHM of the dual bands fit via Equation 5; (d) Normalised integrated LE and HE peak intensities, fit using Equations 6 and 7, respectively. For each analysis, low-temperature and high-temperature trends are respectively identified by regimes I and II. The inset in (c) shows the archetypal form of the temperature dependence of the contributing terms in Equation 5.

The LE and HE peak positions undergo different evolutions in Figure 3(b), due to the superposition of two identified trends. Trend I raises the energy of both peaks, due to a blueshift in the absorption edge with increasing temperature, driven by a combination of thermal expansion and electron-phonon coupling[37,39,40]. LE experiences an additional redshift in regime II at higher temperatures, representing a thermally-induced band splitting[11] superimposed to the aforementioned blueshift. Both effects are activated by phonons with “effective” vibrational energies (ħω) – via electron-phonon coupling – although the respective mode(s) involved are very different. For instance, any phonon mode (acoustic or optical) can raise the lead halide perovskite bandgap energy with increasing temperature[27,37]; however, high-temperature Rashba-like effects must involve modes that break local inversion symmetry[19].

The respective phonon population is governed by Bose−Einstein statistics:

$$n(T) = \frac{1}{e^{\hbar\omega/k_B \mathrm{T}} - 1}, \qquad (2)$$

where k_B is the Boltzmann constant. Warming above absolute zero, low-energy acoustic phonons dominate the initial rise in bandgap energy[27,37,41]. At higher temperatures, optical phonons and spin splitting become more influential, inverting the relative shift in LE[11]. This infers that trend I requires only relatively low phonon energies, while trend II requires relatively high-frequency modes.

Considering the interaction of electrons with the crystal lattice, the temperature dependence of the emission peaks can be reduced to the Bose-Einstein bandgap model[42,43]:

$$E(T) = E_0 + \sum_i A_i \left(\frac{1}{e^{\hbar\omega_i/k_B \mathrm{T}} - 1} + \frac{1}{2}\right). \qquad (3)$$

For up to 3 Bose-Einstein oscillators ω_i (i = 1, 2, 3), A_i represents their weight which, if negative (positive), describes the degree of the energy decrease (increase) with rising temperature, and E_0 is the bandgap energy at 0 K. The evolution of HE will involve the summation of a low-energy acoustic phonon branch (i = 1) and a higher energy optical phonon one (i = 2), with opposite weightings. LE initially follows the shift of HE, though is redshifted by a third relatively high-energy oscillator (i = 3) during trend II. Therefore, the two Bose-

Einstein terms used to account for HE are used as inputs to evaluate their combined influence on LE (fitting parameters in Table S1). The effective phonon frequencies shifting HE ($CsPbBr_3$; $\hbar\omega_1$ = 3.8 meV, $\hbar\omega_2$ = 7.0 meV, and $MAPbBr_3$; $\hbar\omega_1$ = 3.6 meV, $\hbar\omega_2$ = 6.4 meV) are estimated to be far lower than the phonons driving the LE redshift ($CsPbBr_3$; $\hbar\omega_3$ = 14.7 meV, and $MAPbBr_3$; $\hbar\omega_3$ = 11.3 meV). We note the potential involvement of high-energy Raman active optical modes nearing this energy (Figure S3 and S4), whose population will be relatively small below 100 K, in line with the model. Interestingly, the HE and LE peaks in Figure 3(b) approach an intrinsic energy-split near zero temperature[11]; ΔE_{0K} = 30 meV for $CsPbBr_3$, while ΔE_{0K} = 55 meV for $MAPbBr_3$. While dynamic effects arising from thermal fluctuations are suppressed with decreasing temperature, and vanish completely at 0 K, this does not mean that all dynamic effects vanish in quantum systems. Even at absolute zero there are dynamic fluctuations arising from quantum zero-point motion. This comes from predictions made for the perovskites under consideration[19] and are based on the intrinsic dynamic disorder and peak energy splitting at 0 K. More generally, quantum zero-point fluctuations are known to play a major role in other perovskite materials, with the best known example being $SrTiO_3$, which is a quantum paraelectric in which quantum fluctuations stabilise the paraelectric phase compared to the ferroelectric phase[44]. Alternatively, in the absence of clear structural data for these materials near 0 K, the energy split may potentially come about by a loss of centrosymmetry in the crystal structure. However, because the dual peak evolution is common to both all-inorganic $CsPbBr_3$ and hybrid $MAPbBr_3$ materials, this result reinforces the interpretation of “dynamical” spin splitting in the Cs case, as MA statically breaks inversion symmetry due to the dipole in the MA molecule, whereas Cs does not statically break inversion symmetry (i.e. spherical atom). That both perovskite exhibit the same behaviour shows that with the inclusion of dynamics, the physics becomes the same, dominated by the dynamical spin splitting.

Assessing the temperature-dependent emission broadening in Figure 3(c), the intrinsic FWHM (Γ_0) of both perovskites grow with increasing temperatures. Here, an evaluation of the $MAPbBr_3$ HE FWHM evolution is omitted given its complicated asymmetric lineshape in the low-temperature range (Figure S2). Notably, in Figure 3(c), the LE emission in $CsPbBr_3$ broadens faster than HE with rising temperature, suggesting enhanced carrier scattering in these bands. The temperature-dependent excitonic linewidth of band-to-band transitions within semiconductors[32,45] is relatively well understood, being described by

$$\begin{aligned} \Gamma(T) &= \Gamma_0 + \Gamma_{ac} + \Gamma_{LO} + \Gamma_{imp} \\ &= \Gamma_0 + \gamma_{ac} T + \gamma_{LO} n(T) + \gamma_{imp} e^{-E_b/k_B \mathrm{T}}. \end{aligned} \tag{4}$$

The second and third terms (Γ_{ac} and Γ_{LO}) respectively describe the trends ascribed to acoustic and LO-phonon (Fröhlich) scattering, with coupling strengths γ_{ac} and γ_{LO}. The fourth term accounts for the scattering from ionized impurities, with average binding energy E_b. Below 75 K, the linear Γ_{ac} component – involving low-energy acoustic phonons – will dominate the broadening. The gradient of the of the FWHM of all peaks is essentially flat in regime I, in-line with negligible contributions from the γ_{ac} term[32,46–48] and is omitted for simplicity. The small sublinear feature in LE below 100 K for both $CsPbBr_3$ and $MAPbBr_3$ resembles the influence of Γ_{imp} (inset of Figure 3(d)), but does not appear in HE. Because it is unlikely that ionised impurities will selectively scatter carriers residing only in the LE bands, this feature is suggested to have other origins and we omit for simplicity[32]. There is a group of distinct LO-optical vibrations expected to interact with charge carriers[49] (Figure S3 and S4) with energies close to 17 meV (~140 cm^{-1}), and are energetically stable down to cryogenic temperatures. Therefore, we adopt a simplified model to fit our data[32], dependent on two dominant components:

$$\Gamma(T) = \Gamma_0 + \frac{\gamma_{LO}}{e^{\hbar\omega_{LO}/k_B \mathrm{T}} - 1}\,. \tag{5}$$

For the LE band, a temperature invariant γ_{LO} broadening parameter may not fully describe its behaviour over the temperature range explored, as its nature is dependent on the phonon population. However, the broadening of LE above 100 K is fairly linear in both $CsPbBr_3$ and $MAPbBr_3$, being agreeably fit by a fixed γ_{LO} parameter. We note that analogous models have been used for heavy- and light-hole VB splitting in strained epitaxial semiconductors and quantum wells[50], which experience temperature-dependent changes in their band dispersion at the high-symmetry points.

Through Equation 5 we estimate the relative strength of the Fröhlich coupling arising in the two recombination pathways in CsPbBr$_3$; γ_{LO} is determined to be 54 ± 5 meV for the direct HE transition, while the LE linewidth broadening generates a value of 78 ± 8 meV. For the LE peak of MAPbBr$_3$, we derive a value of γ_{LO} = 64 ± 6 meV. The large difference in coupling strength between the direct and spin-split bands in CsPbBr$_3$ is expected within a Fröhlich coupling model which corrects for SOC, as described previously. For lead bromide perovskites, γ_{LO} values generally near 60 meV[32,51,52]. However, the sensitivity of the LE emission to the sample preparation[11] may explain the large spread in γ_{LO} values reported[47,48,52–54] from low-temperature PL analysis of this materials, reaching as high as 130 meV[55].

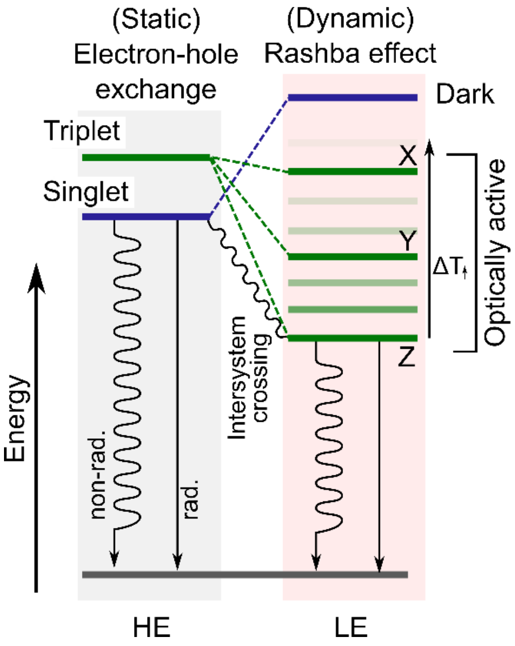

Figure 4: The expected fine structure[56] of the band-edge excitons considering short- and long-range electron–hole exchange (left) and then including Rashba-like effects[57] with symmetry breaking along the z direction (right), under orthorhombic symmetry. In the split states, the exciton separates into three bright states and a high-energy dark state. Intersystem crossing will depend on the relative population of the low-energy spin split triplet states, which is governed by the crystal temperature.

Figure 3(a) shows that the relative weighting of the LE band in the dual PL spectra significantly grows in both $CsPbBr_3$ and $MAPbBr_3$ perovskites upon cooling, which is tracked in Figure 3(d) (note the $MAPbBr_3$ HE intensity is derived from fully integrating the HE band, using two Gaussian peaks). First considering the more standard characteristic of the LE bands, the initial intensity (I_0) decreases above 0 K due to thermally activated quenching (estimated via a single dominant non-radiative channel), commonly described by an Arrhenius expression:

$$I(T) = \frac{I_0}{1 + ae^{-E_a/k_B\mathrm{T}}}\,, \qquad (6)$$

where a is the ratio of non-radiative and radiative probabilities and E_a is the activation energy of the quenching channel. Applying Equation 6 to the temperature dependence of the LE intensity yields an activation energy of 11 meV for $CsPbBr_3$ and 18 meV for $MAPbBr_3$ (Table S2).

The temperature dependence of the HE emissions, on the other hand, is more complex; the HE peak intensity maximises under 100 K and begins to quench moving to either lower (regime I) and higher (regime II) temperatures. At higher temperatures, the HE intensity decrease is similar to LE, manifesting via indiscriminate thermally activated non-radiative carrier recombination. In regime I, however, the system is subject to another non-radiative channel which becomes significant upon cooling toward 0 K. The Arrhenius fitting can be modified to include the second quenching term, whereby

$$I(T) = \frac{I_0}{1 + a_1 e^{-\frac{E_{a1}}{k_B\mathrm{T}}} + \; a_2 e^{-\frac{E_{a2}}{k_B\mathrm{T}}}}\,. \qquad (7)$$

The two competing processes ($a_1 > 0;\ a_2 < 0$) superimpose to yield a maximum below 100 K, with the fitting parameters provided in Table S2.

The origin of the non-radiative channel quenching in regime I for both $CsPbBr_3$ and $MAPbBr_3$ is difficult to isolate, though it is likely connected to thermally-driven intersystem crossing between the bright low-energy spin-split triplet states and the bright direct transition involving a singlet state[56]. This is because the intersystem crossing between the states must be mediated by phonons, which are depopulated and vanish toward 0 K. Based on the predicted exciton fine structure of $CsPbBr_3$ perovskite[56–59], an energy scheme representing this proposition is displayed in Figure 4. The left and right portions of the scheme represent the static and dynamic cases of the electronic structure, which generate the unperturbed and perturbed band structures in Figure 1, respectively. As shown in Figure 4, thermal energy is required to populate the low-energy Rashba bands and allow reverse intersystem crossing to the static HE transition, thus facilitating a more intense HE emission. This is because the system remains split at 0 K, retaining the lower energy indirect tail states. That is to say, some of the rise in the low-energy emission intensity while cooling in regime I is at the cost of depopulating the radiative high-energy transition.

In summary, we have reported a low-temperature PL analysis of high-quality single crystals of $CsPbBr_3$ and $MAPbBr_3$ emitting a dual emission accounting for Rashba-like effects. We find that a single-band-to-band model no longer accounts for the radiative recombination pathways expressed in this system, due to different physical properties of carriers residing in the split band structure. While the formation of indirect tail states promotes longer radiative lifetimes[14], it ultimately enhances electron-phonon scattering, reducing carrier mobility and leading to a relatively broader low-energy emission. To explain the origin of this behaviour, we connect both the enhancement in the effective mass of carriers residing in the spin-split bands and the requirement for additional scattering to overlap the bands, for recombination. Further, the direct band-edge recombination is quenched near 0 K, which we attribute to the presence of an unpopulated low-energy indirect emission pathway. These findings allow rationalization of previous experimental observations and provide a key to understanding the complex carrier dynamics in bulk spin-split halide perovskites**. Cs = MA, meaning cation independent**.

1. Green, M. A., Ho-Baillie, A. & Snaith, H. J. The emergence of perovskite solar cells. *Nat Photon* **8**, 506–514 (2014).

2. Meredith, P. & Armin, A. Scaling of next generation solution processed organic and perovskite solar cells. *Nature Communications* **9**, 5261 (2018).
3. Kang, J. & Wang, L.-W. High Defect Tolerance in Lead Halide Perovskite $CsPbBr_3$. *The Journal of Physical Chemistry Letters* **8**, 489–493 (2017).
4. Walsh, A. & Zunger, A. Instilling defect tolerance in new compounds. *Nature Materials* **16**, 964–967 (2017).
5. Miyata, K., Atallah, T. L. & Zhu, X. Y. Lead halide perovskites: Crystal-liquid duality, phonon glass electron crystals, and large polaron formation. *Science Advances* **3**, e1701469 (2017).
6. Miyata, K. *et al.* Large polarons in lead halide perovskites. *Science Advances* **3**, e1701217 (2017).
7. Frost, J. M. & Walsh, A. What Is Moving in Hybrid Halide Perovskite Solar Cells? *Accounts of Chemical Research* **49**, 528–535 (2016).
8. Zhu, H. *et al.* Screening in crystalline liquids protects energetic carriers in hybrid perovskites. *Science* **353**, 1409–1413 (2016).
9. Zhu, X.-Y. & Podzorov, V. Charge Carriers in Hybrid Organic–Inorganic Lead Halide Perovskites Might Be Protected as Large Polarons. *J. Phys. Chem. Lett.* **6**, 4758–4761 (2015).
10. Stranks, S. D. *et al.* Electron-Hole Diffusion Lengths Exceeding 1 Micrometer in an Organometal Trihalide Perovskite Absorber. *Science* **342**, 341–344 (2013).
11. Wu, B. *et al.* Indirect tail states formation by thermal-induced polar fluctuations in halide perovskites. *Nature Communications* **10**, 484 (2019).
12. Niesner, D. *et al.* Structural fluctuations cause spin-split states in tetragonal $(CH_3NH_3)PbI_3$ as evidenced by the circular photogalvanic effect. *Proceedings of the National Academy of Sciences* **115**, 9509–9514 (2018).

13. McKechnie, S. *et al.* Dynamic symmetry breaking and spin splitting in metal halide perovskites. *Physical Review B* **98**, 085108 (2018).
14. Zheng, F., Tan, L. Z., Liu, S. & Rappe, A. M. Rashba Spin–Orbit Coupling Enhanced Carrier Lifetime in CH $_3$ NH $_3$ PbI $_3$. *Nano Letters* **15**, 7794–7800 (2015).
15. Wang, T. *et al.* Indirect to direct bandgap transition in methylammonium lead halide perovskite. *Energy & Environmental Science* **10**, 509–515 (2017).
16. Isarov, M. *et al.* Rashba Effect in a Single Colloidal CsPbBr $_3$ Perovskite Nanocrystal Detected by Magneto-Optical Measurements. *Nano Lett.* **17**, 5020–5026 (2017).
17. Niesner, D. *et al.* Giant Rashba Splitting in CH 3 NH 3 PbBr 3 Organic-Inorganic Perovskite. *Phys. Rev. Lett.* **117**, 126401 (2016).
18. Röhm, H. *et al.* Ferroelectric Properties of Perovskite Thin Films and Their Implications for Solar Energy Conversion. *Advanced Materials* 1806661 (2019). doi:10.1002/adma.201806661
19. Monserrat, B. & Vanderbilt, D. Phonon-assisted spin splitting in centrosymmetric crystals. *arXiv:1711.06274 [cond-mat]* (2017).
20. Frohna, K. *et al.* Inversion symmetry and bulk Rashba effect in methylammonium lead iodide perovskite single crystals. *Nature Communications* **9**, 1829 (2018).
21. Zhang, X., Shen, J.-X., Wang, W. & Van de Walle, C. G. First-Principles Analysis of Radiative Recombination in Lead-Halide Perovskites. *ACS Energy Letters* **3**, 2329–2334 (2018).
22. Azarhoosh, P., McKechnie, S., Frost, J. M., Walsh, A. & van Schilfgaarde, M. Research Update: Relativistic origin of slow electron-hole recombination in hybrid halide perovskite solar cells. *APL Materials* **4**, 091501 (2016).
23. Dar, M. I. *et al.* Origin of unusual bandgap shift and dual emission in organic-inorganic lead halide perovskites. *Science Advances* **2**, e1601156 (2016).

24. Stoumpos, C. C. *et al.* Crystal Growth of the Perovskite Semiconductor CsPbBr 3 : A New Material for High-Energy Radiation Detection. *Crystal Growth & Design* **13**, 2722–2727 (2013).
25. Yaffe, O. *et al.* Local Polar Fluctuations in Lead Halide Perovskite Crystals. *Physical Review Letters* **118**, 136001 (2017).
26. Thu Ha Do, T. *et al.* Optical study on intrinsic exciton states in high-quality CH 3 NH 3 PbBr 3 single crystals. *Physical Review B* **96**, 075308 (2017).
27. Diroll, B. T., Zhou, H. & Schaller, R. D. Low-Temperature Absorption, Photoluminescence, and Lifetime of CsPbX $_3$ (X = Cl, Br, I) Nanocrystals. *Advanced Functional Materials* **28**, 1800945 (2018).
28. Sebastian, M. *et al.* Excitonic emissions and above-band-gap luminescence in the single-crystal perovskite semiconductors CsPbBr3 and CsPbCl3. *Physical Review B - Condensed Matter and Materials Physics* **92**, 235210 (2015).
29. Yu, Z.-G. Rashba Effect and Carrier Mobility in Hybrid Organic–Inorganic Perovskites. *J. Phys. Chem. Lett.* **7**, 3078–3083 (2016).
30. Yu, Z.-G. The Rashba effect and indirect electron–hole recombination in hybrid organic–inorganic perovskites. *Phys. Chem. Chem. Phys.* **19**, 14907–14912 (2017).
31. Rakita, Y. *et al.* Low-Temperature Solution-Grown CsPbBr3 Single Crystals and Their Characterization. *Crystal Growth and Design* **16**, 5717–5725 (2016).
32. Wright, A. D. *et al.* Electron-phonon coupling in hybrid lead halide perovskites. *Nature Communications* **7**, 11755 (2016).
33. Feynman, R. P. Slow Electrons in a Polar Crystal. *Physical Review* **97**, 660–665 (1955).
34. Yu A Bychkov & ÉI Rashba. Properties of a 2D electron gas with lifted spectral degeneracy. *JETP lett* **39**, 78 (1984).

35. Monserrat, B. & Vanderbilt, D. Temperature dependence of the bulk Rashba splitting in the bismuth tellurohalides. *Physical Review Materials* **1**, 054201 (2017).
36. Covaci, L. & Berciu, M. Polaron Formation in the Presence of Rashba Spin-Orbit Coupling: Implications for Spintronics. *Physical Review Letters* **102**, 186403 (2009).
37. Saidi, W. A., Poncé, S. & Monserrat, B. Temperature Dependence of the Energy Levels of Methylammonium Lead Iodide Perovskite from First-Principles. *The Journal of Physical Chemistry Letters* **7**, 5247–5252 (2016).
38. Li, Z., Ma, Z., Wright, A. R. & Zhang, C. Spin-orbit interaction enhanced polaron effect in two-dimensional semiconductors. *Applied Physics Letters* **90**, 112103 (2007).
39. Milot, R. L., Eperon, G. E., Snaith, H. J., Johnston, M. B. & Herz, L. M. Temperature-Dependent Charge-Carrier Dynamics in $CH_3NH_3PbI_3$ Perovskite Thin Films. *Advanced Functional Materials* **25**, 6218–6227 (2015).
40. Foley, B. J. *et al.* Temperature dependent energy levels of methylammonium lead iodide perovskite. *Applied Physics Letters* **106**, 243904 (2015).
41. Saidi, W. A. & Kachmar, A. Effects of Electron–Phonon Coupling on Electronic Properties of Methylammonium Lead Iodide Perovskites. *The Journal of Physical Chemistry Letters* **9**, 7090–7097 (2018).
42. Lautenschlager, P., Garriga, M., Logothetidis, S. & Cardona, M. Interband critical points of GaAs and their temperature dependence. *Physical Review B* **35**, 9174–9189 (1987).
43. Bhosale, J. *et al.* Temperature dependence of band gaps in semiconductors: Electron-phonon interaction. *Physical Review B* **86**, 195208 (2012).
44. Müller, K. A. & Burkard, H. SrTiO3 : An intrinsic quantum paraelectric below 4 K. *Phys. Rev. B* **19**, 3593–3602 (1979).
45. Rudin, S. & Reinecke, T. L. Temperature-dependent exciton linewidths in semiconductor quantum wells. *Physical Review B* **41**, 3017–3027 (1990).

46. Han, Q., Wu, W., Liu, W., Yang, Q. & Yang, Y. Temperature-dependent photoluminescence of CsPbX3 nanocrystal films. *Journal of Luminescence* **198**, 350–356 (2018).

47. Ramade, J. *et al.* Exciton-phonon coupling in a CsPbBr3 single nanocrystal. *Applied Physics Letters* **112**, 072104 (2018).

48. Wolf, C. & Lee, T.-W. Exciton and lattice dynamics in low-temperature processable CsPbBr3 thin-films. *Materials Today Energy* **7**, 199–207 (2018).

49. Schlipf, M., Poncé, S. & Giustino, F. Carrier Lifetimes and Polaronic Mass Enhancement in the Hybrid Halide Perovskite CH 3 NH 3 PbI 3 from Multiphonon Fröhlich Coupling. *Physical Review Letters* **121**, 086402 (2018).

50. Lee, J., Koteles, E. S. & Vassell, M. O. Luminescence linewidths of excitons in GaAs quantum wells below 150 K. *Physical Review B* **33**, 5512–5516 (1986).

51. Ghosh, S. *et al.* Phonon Coupling with Excitons and Free Carriers in Formamidinium Lead Bromide Perovskite Nanocrystals. *J. Phys. Chem. Lett.* **9**, 4245–4250 (2018).

52. Zhang, F. *et al.* Silica coating enhances the stability of inorganic perovskite nanocrystals for efficient and stable down-conversion in white light-emitting devices. *Nanoscale* **10**, 20131–20139 (2018).

53. Qiuju Han, Wu, W., Weilong Liu & Qingxin Yang. Temperature-dependent photoluminescence of CsPbX3 nanocrystal films. *Journal of Luminescence* **198**, 350–356 (2018).

54. Lee, S. M. *et al.* Temperature-Dependent Photoluminescence of Cesium Lead Halide Perovskite Quantum Dots: Splitting of the Photoluminescence Peaks of $CsPbBr_3$ and $CsPb(Br/I)_3$ Quantum Dots at Low Temperature. *J. Phys. Chem. C* **121**, 26054–26062 (2017).

55. Wei, K. *et al.* Temperature-dependent excitonic photoluminescence excited by two-photon absorption in perovskite CsPbBr_3 quantum dots. *Opt. Lett.* **41**, 3821 (2016).
56. Becker, M. A. *et al.* Bright triplet excitons in caesium lead halide perovskites. *Nature* **553**, 189–193 (2018).
57. Sercel, P. C. *et al.* Exciton Fine Structure in Perovskite Nanocrystals. *Nano Lett.* **19**, 4068–4077 (2019).
58. Utzat, H. *et al.* Coherent single-photon emission from colloidal lead halide perovskite quantum dots. *Science* **363**, 1068–1072 (2019).
59. Tamarat, P. *et al.* The ground exciton state of formamidinium lead bromide perovskite nanocrystals is a singlet dark state. *Nature Materials* **18**, 717–724 (2019).

Acknowledgements The authors acknowledge financial support from the Research Foundation-Flanders (FWO, Grant Nos. 12Y7218N, G.0B39.15, G.0197.11 and 12O3719N postdoctoral fellowship to J.A.S., C.M., H.Y. and E.D.), KU Leuven Research Fund (C14/15/053), the Flemish government through long term structural funding Methusalem (CASAS2, Meth/15/04), the Hercules foundation (HER/11/14), and the Belgian Federal Science Policy Office (IAP-VII/05). The research leading to these results has received funding from the European Research Council under the European Union's Seventh Framework Programme (FP/2007-2013)/ERC Grant Agreement (Grant No. 307523). B.M. acknowledges support from the Winton Programme for the Physics of Sustainability and from Robinson College, Cambridge, and the Cambridge Philosophical Society for a Henslow Research Fellowship. B.W. acknowledges support from the National Natural Science Foundation of China (NFSC) (grant No. 51802331), Guangdong Provincial Key Laboratory of Optical Information Materials and Technology (Grant No. 2017B030301007) and the 111 Project. T.K. acknowledges support from the Impuls- und Vernetzungsfonds der Helmholtz Gemeinschaft via the project PEROSEED. We are grateful to the UK Materials and Molecular Modelling Hub for computational resources, which is partially funded by EPSRC (EP/P020194/1). T.C.S. acknowledges the support from the Ministry of Education AcRF Tier 2 grant MOE2016-T2-1-034 and from the Singapore National Research Foundation Investigatorship NRF-NRFI-2018-04. J.A.S. thanks Prof. Chao Zhang for his helpful discussions.

TOC graphical entry